Engineering 58 (2026) 291–301

Contents lists available at ScienceDirect

Engineering

journal homepage: www.elsevier.com/locate/eng

Research
Engineering Management—Article

A Coupled Elastohydrodynamic–Acoustic Framework for High-Resolution Ultrasonic Measurement of Dynamic Film Thickness in Lubricated Contacts

Pan Dou [a,b], Yayu Li [a], Suhaib Ardah [b], Tonghai Wu [a,*], Min Yu [b], Thomas Reddyhoff [b], Yaguo Lei [a], Daniele Dini [b]

[a] Key Laboratory of Education Ministry for Modern Design and Rotor-Bearing System, Xi'an Jiaotong University, Xi'an 710049, China
[b] Department of Mechanical Engineering, Imperial College London, London SW7 2AZ, UK

ARTICLE INFO

Article history:
Received 13 July 2025
Revised 14 January 2026
Accepted 20 January 2026
Available online 28 January 2026

Keywords:
Rolling bearing
Central film thickness
Ultrasonic measurement
Elastohydrodynamic lubrication
Cavitation

ABSTRACT

The thickness of the lubricating film plays a vital role in the operational efficiency and reliability of rolling bearings. Ultrasonic reflection techniques offer a promising noninvasive approach for the *in situ* evaluation of lubricant films. However, accurate identification of the central film thickness remains challenging because of several complex factors, which include dynamic fluctuations, localized elastic deformation, cavitation effects, and variations in the oil supply. In this study, a comprehensive theoretical and numerical framework for elucidating the effects of these factors on ultrasonic wave propagation in lubricated contacts is presented. Numerical simulations in which the elastohydrodynamic lubrication (EHL) regime and cavitation-induced effects are considered are carried out to obtain surface deformation profiles and identify cavitation regions. High-fidelity acoustic simulations are subsequently conducted to interpret the reflected ultrasound data. The reflection coefficient distribution exhibits a symmetric "double peak with central valley" pattern that is induced by the combined effect of the contact geometry and the EHL-induced oil film thickness distribution. Cavitation causes the central valley to shift toward the inlet region and increases the reflection coefficient. Accordingly, the central film thickness is extracted from the distribution of the reflection coefficient under different operating conditions. Experimental validation using both glass–oil–steel and steel–oil–steel bearing setups confirms the effectiveness of the proposed method. The high-resolution fluorescence measurement that is adopted in the glass–oil–steel configuration validates the simulation of the reflection coefficient distribution. Furthermore, theoretical EHL calculations are performed for the steel–oil–steel configuration to validate the measurement accuracy for the central oil film thickness.

© 2026 THE AUTHORS. Published by Elsevier LTD on behalf of Chinese Academy of Engineering and Higher Education Press Limited Company. This is an open access article under the CC BY-NC-ND license (http://creativecommons.org/licenses/by-nc-nd/4.0/).

1. Introduction

Rolling bearings, which serve as the "joints" of machines, have advantages such as a low friction coefficient, high radial load capacity, and high rotational accuracy; hence, they are used as the core supporting components of large rotating equipment. The operational reliability of the bearings depends strongly on the lubricant films between the rollers and the inner and outer rings. These oil films are present in microscale contact regions and supports all loads; therefore, they are extremely small and thin. Such ultrathin films are fragile under extreme conditions and often rupture, which results in solid wear in roller bearings. Accordingly, the lubricant film thickness can be used as a preliminary index for most rolling bearing failures. It provides a reliable reference for ensuring the operational stability of rotating equipment [1,2]. Many researchers have therefore been motivated to inspect oil films; however, this remains a significant challenge because of the complex characteristics of the films, including the microscale, complex geometry, cavitation, and dynamic deformations.

Various measurement techniques, such as electrical, optical, and ultrasonic techniques, have been proposed for measuring lubricant film thickness. Although electrical and optical methods can be used to measure lubricant film thickness under the elastohydrodynamic lubrication (EHL) conditions, they require strict electromagnetic shielding or the demand for at least one side of

* Corresponding author.
E-mail address: tonghai.wu@mail.xjtu.edu.cn (T. Wu).

https://doi.org/10.1016/j.eng.2026.01.014
2095-8099/© 2026 THE AUTHORS. Published by Elsevier LTD on behalf of Chinese Academy of Engineering and Higher Education Press Limited Company.
This is an open access article under the CC BY-NC-ND license (http://creativecommons.org/licenses/by-nc-nd/4.0/).

the friction pair to be transparent, thus limiting their applicability to laboratory environments [3,4]. The linear propagation and strong penetration of ultrasound make it the most promising technique for the nondestructive, noninvasive measurement of film thickness in industrial settings [5]. Advances in acoustic measurement models have enabled the successful application of ultrareflection-based technology in systems such as cylinder linear-piston ring systems and fuel pumps [6,7]. However, its adoption in rolling bearings remains limited because of challenges in achieving sufficient spatial resolution for measurements.

To obtain high-resolution measurements, various types of ultrasonic sensors, including water-focused sensors, thin-film sensors, and piezoelectric ceramic sensors, have been explored. However, water-focused sensors are bulky and difficult to install, whereas thin-film sensors involve complex fabrication processes; thus, both types of sensors are challenging to apply in practical engineering scenarios [8,9]. In contrast, Clarke et al. [10] proposed the promising approach of directly attaching adhesive piezoelectric ceramic sensors to the outer surfaces of roller bearings. Owing to the ability to cut and trim piezoelectric ceramic sensors to smaller widths, combined with the ease of installation of these sensors, they have already been applied in various real-world engineering cases, such as large-scale rolling bearings [11]. Nevertheless, the width of the contact area to be measured remains larger than the width of the sensor.

To elucidate the relationship between the central film thickness reflection coefficient and the overall sensor reflection coefficient from measurements, thereby capturing the coupled effects of multiple physical phenomena, successful attempts have been made using physics-based ray models [9], simulation-based acoustic models [12], and data-driven system identification methods [13]. The challenge in elucidating this relationship is attributable primarily to two factors: First, although the equivalent deformation assumption is widely adopted in EHL calculations because of its simplicity and computational convenience, it does not accurately capture the real profile geometry, thus resulting in discrepancies in ultrasonic wave scattering [9]. Second, the length of the inlet region and cavitation are typically observed in rolling bearings, and the substantial difference between the reflection coefficients at the steel–air and steel–oil film interfaces significantly alters the ultrasonic reflection behavior, thereby introducing additional spurious reflections at the oil film–air boundary [14]. The coupling of these two effects leads to deviations in the correlation between the reflection coefficients of the central film thickness (R_c) and the overall sensor (R_{sc}), which ultimately leads to measurement errors.

To address this issue, numerical elastohydrodynamic–acoustic modeling is adopted in this study to interpret reflected ultrasound data under complex EHL conditions. First, an EHL numerical simulation in which cavitation is considered is conducted to obtain critical information on line-contact lubrication. Afterward, a high-fidelity acoustic simulation is accurately carried out to investigate the influence mechanisms of EHL, cavitation, inlet region length, speed, and load on ultrasonic reflection. This enables the central film thickness to be determined from the reflection coefficient distribution under varying operating conditions. Finally, experimental validation is conducted using a roller bearing test rig. The simulation results are compared with fluorescence-based measurements, and the accuracy of the central film thickness is validated against theoretical EHL predictions. An overview of the proposed methodology is illustrated in Fig. 1.

2. Methods

An EHL simulation is first performed to obtain detailed information on the deformed contact profile, oil film thickness distribution, positions of cavitated regions, and hydrodynamic pressure field (Section 2.1). High-fidelity acoustic simulations are subsequently conducted to analyze the effects of the outlet and inlet region lengths, load, and rotational speed on the ultrasonic reflection behavior (Section 2.2). On the basis of these results, a method is proposed for determining the central film thickness using ultrasonic reflections (Section 2.3).

2.1. EHL simulation with consideration of cavitation

EHL typically occurs in rolling element bearings that operate under high-load and high-speed conditions. The distribution of the lubricant film is governed by a complex interplay of factors, which most notably include the hydrodynamic pressure that is generated in the confined film and the pressure-induced elastic deformation of the contacting surfaces. The lubricant film within a rolling or sliding contact is generally segmented into three distinct regions: the inlet zone, Hertzian contact zone, and outlet zone. In the Hertzian region, which is located at the center of contact, the oil film thickness remains relatively uniform until it sharply decreases near the outlet region. In the inlet region, the geometry and length of the lubricant film significantly affect pressure buildup; a longer inlet enhances the lubrication stability and reduces the risk of lubrication failure. In the outlet region, a rapid pressure drop may cause cavitation, thereby deteriorating lubrication performance and accelerating wear. To accurately determine the film thickness and pressure distribution, a cavitation-inclusive EHL simulation (Fig. 2) is conducted.

The distribution of the hydrodynamic pressure and lubricant film content within the lubricated line contact is described by the $p-\theta$ generalized Reynolds equation (GRE), which accounts for the combined effect of surface kinematics, film thickness variations $h(x)$, and spatial changes in lubricant properties such as viscosity $\eta(x)$ and density $\rho(x)$ (x is the coordinate along the entrainment direction). Given the lower- and upper-surface contact velocities along the x-direction (u_1 and u_2, respectively, as shown in Fig. 2), the modified $p-\theta$ GRE is expressed in its conservative form as follows [15]:

$$\frac{\partial}{\partial x}\left(\epsilon\frac{\partial p}{\partial x}\right)=\frac{\partial(\theta\rho_x^*)}{\partial x} \tag{1}$$

where p denotes the local hydrodynamic pressure and θ denotes the film fraction that represents the liquid volume present in the biphasic mixture caused by cavitation. The coefficients ϵ and ρ_x^* correspond to the effective Poiseuille and Couette mass-flux contributions in Eq. (1), respectively, and account for spatial variations in lubricant viscosity $\eta(z)$ and density $\rho(z)$ across the film thickness. These coefficients are defined as follows:

$$\begin{cases}\epsilon=\frac{\eta_e}{\eta_e'}\rho'-\rho''\\ \rho_x^*=\rho_e u_1+\eta_e\rho'(u_2-u_1)\end{cases} \tag{2}$$

where the effective density ρ_e and viscosity η_e integrals across the lubricant film $z\in[z_1,z_2]$, where z_1 and z_2 correspond to the positions of the lower and upper solid surfaces bounding the film, respectively, are given by

$$\begin{cases}\rho_e=\int_{z_1}^{z_2}\rho\,\mathrm{d}z\\ \frac{1}{\eta_e}=\int_{z_1}^{z_2}\frac{\mathrm{d}z}{\eta}\\ \frac{1}{\eta_e'}=\int_{z_1}^{z_2}\frac{z\mathrm{d}z}{\eta}\end{cases} \tag{3}$$

and the auxiliary density–viscosity coupling terms are defined as follows:

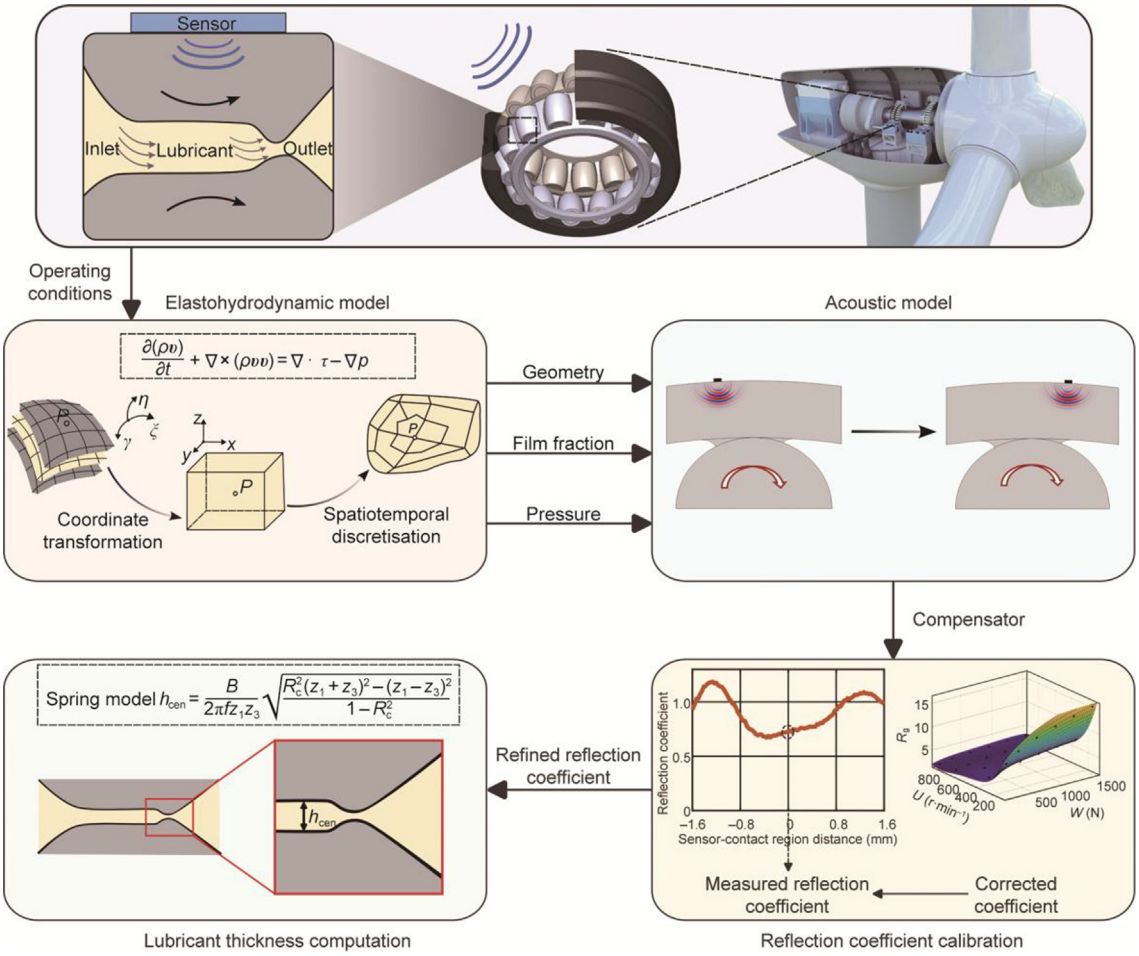

Fig. 1. Overview of a coupled elastohydrodynamic–acoustic framework for the high-resolution ultrasonic measurement of dynamic film thickness in lubricated contacts. In the conservative form of the Navier–Stokes momentum equation, ρ is the fluid density, $\boldsymbol{v}$ is the velocity field, $\rho\boldsymbol{vv}$ is the momentum flux tensor, p is the pressure, τ is the viscous stress tensor, ∇ is the spatial gradient operator, $\nabla\cdot$ denotes divergence and P is a node located in the computational grid. (ξ,η,γ) and (x,y,z) are coordinates associated with a curvilinear and Cartesian computational grid systems, respectively. h_{cen} denotes the central film thickness in a lubricated contact. In the spring model, f is the frequency of the sound wave, R_c is the reflection coefficient in the contact area, and B is the bulk modulus of the lubricant layer. The term z denotes the acoustic impedance of the medium, with subscripts 1 and 3 representing the tribopair materials on either side of the lubricant film. Furthermore, R_g is the correction factor, U is the rotational speed, and W is the applied load.

$$\begin{cases} \rho' = \int_{z_1}^{z_2} \rho \int_{z_1}^{z} \frac{\mathrm{d}z'}{\eta}\mathrm{d}z \\ \rho'' = \int_{z_1}^{z_2} \rho \int_{z_1}^{z} \frac{z'\mathrm{d}z'}{\eta}\mathrm{d}z \end{cases} \tag{4}$$

To enforce the mass conservation principles within the lubricated domain, this study employs the Elrod–Adams $p-\theta$ cavitation algorithm [16], which incorporates the Jakobsson–Floberg–Olsson (JFO) conditions as a foundation for defining cavitation boundaries, is used in this study. The associated complementary boundary conditions are specified as follows:

$$(p-p_{cav})(1-\theta)=0 \rightarrow \begin{cases} p>p_{cav} \rightarrow \theta=1, & \text{pressured zones} \\ p=p_{cav} \rightarrow 0\le\theta<1, & \text{cavitated zones} \end{cases} \tag{5}$$

where p_{cav} represents the vapor-phase cavitation pressure, which corresponds to the pressure within the cavitation region. A value of $\theta=1$ corresponds to a fully liquid-filled region, whereas $0\le\theta<1$ corresponds to a cavitated region.

In line-contact lubrication, the characteristic dimensions and curvature radii of the contacting bodies are much larger than the width of the contact zone. This geometric setup enables the contact to be modeled under plane strain conditions, which are mathematically equivalent to those of a flat elastic medium that is experiencing distributed pressure. The resulting film thickness distribution $h(x)$ along the one-dimensional contact can be expressed as follows [17]:

$$h(x)=h_0+\frac{x^2}{2R'}+v(x) \tag{6}$$

where h_0 denotes the initial film thickness in the absence of elastic deformation and R' represents the equivalent curvature radius of the contacting surfaces. The elastic surface deformation v that is induced by a pressure distribution $p(s)$ acting on the line region Ω is calculated using the Flamant solution, which is expressed as follows:

$$v(x)=-\frac{2}{\pi E'}\int_{\Omega} p(s)\ln(x-s)^2\mathrm{d}s \tag{7}$$

where s serves as the integration variable representing the coordinate of the distributed pressure acting along the contact zone, E' is the equivalent elastic modulus, and the integration is performed over the contact domain.

The EHL model that is adopted in this study follows the computational framework that is presented in Ref. [17], where the governing equations are discretized using finite volume methods

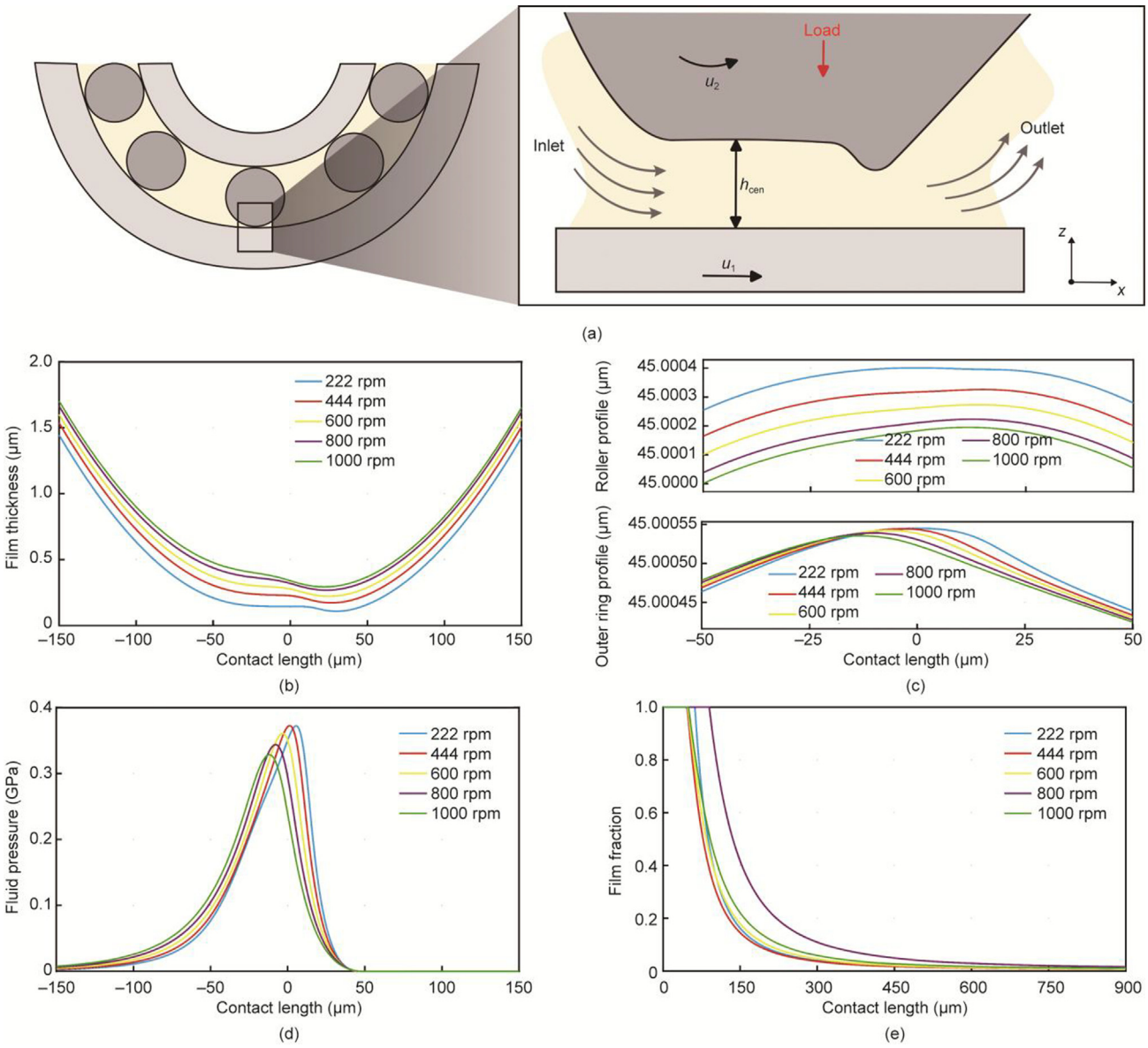

Fig. 2. EHL numerical simulation under line-contact lubrication conditions. (a) Schematic illustration of fluid film thickness and pressure distribution in an EHL contact; (b) equivalent deformation profile of the contact that is based on EHL numerical calculations; (c) actual deformation profile, which shows elastic deformation under loading; (d) pressure distribution within the lubricated contact region; (e) film fraction distribution, which indicates the presence of full film and cavitation regions. u_1 and u_2: the lower- and upper-surface contact velocities along the x-direction; rpm: revolutions per minute.

(FVMs). The nonlinearities exhibited by the system of governing equations are addressed using the semisystem approach integrated within the iterative solution. In the simulation framework, the point Gauss–Seidel method with Aitken acceleration (PGMA) is used. The PGMA scheme increases the convergence stability of traditional partitioned solvers by adaptively adjusting the scalar relaxation factor within each iterative step, guided by the residuals computed from both the current and preceding iterative steps. For comprehensive details on the implementation of both the semisystem strategy and the PGMA technique, including their contributions to accelerating EHL simulation convergence and revamping numerical robustness under heavy load conditions, the reader is referred to Refs. [17–19]. Table 1 [20] summarizes the key parameters of the roller and outer ring that are used in this study.

The interaction between the roller and the outer ring is often idealized as a simplified contact model that comprises an equivalent cylindrical body against a perfectly rigid foundation. However, this simplification deviates from the true geometrical configuration of the rolling element–raceway contact. Most importantly, the propagation behavior of ultrasonic waves is sensitive to geometric details, and equivalent shapes may fail to capture the wave behavior accurately. Therefore, reconstructing actual geometric deformation profiles on the basis of accurate geometrical relationships is vital. On the basis of the equivalent deformation field, the individual deformation contributions from the roller and the inner surface of the outer ring can be calculated as follows:

$$v_{\mathrm{r}}(x) = v(x)\frac{(1-\mu_{\mathrm{r}}{}^2)E'}{2E_{\mathrm{r}}} \tag{8}$$

$$v_{\mathrm{ri}}(x) = v(x)\frac{(1-\mu_{\mathrm{ri}}{}^2)E'}{2E_{\mathrm{ri}}} \tag{9}$$

Table 1
Parameters for the EHL simulation of the roller and ring contact.

Item	Radius (mm)	Material	Material elastic modulus (GPa)	Poisson's ratio	Lubricant [20]
Roller	6.25	Steel	210	0.293	PAO4
Outer ring	45 (inner radius)	Steel	210	0.293	PAO4

PAO4: polyalphaolefin 4.

where $v_r(x)$ and $v_{ri}(x)$ denote the deformation fields of the roller and the inner surface of the outer ring, respectively. Furthermore, E_r and E_{ri} represent the elastic moduli of the roller and outer ring respectively; and μ_r and μ_{ri} denote their respective Poisson's ratios, respectively.

By leveraging the deformation of the inner surface of the outer ring and its initial geometric profile, the true geometric profile of the inner surface of the outer ring, which is denoted as $d_{ri}(x)$, can be calculated as follows:

$$d_{ri}(x) = R_{ri} - \sqrt{R_{ri}^2 - x^2} + v_{ri}(x) \tag{10}$$

where R_{ri} represents the inner radius of the outer ring.

The true geometric profile of the outer surface of the outer ring, which is denoted by $d_{ro}(x)$, can be determined as follows:

$$d_{ro}(x) = R_{ro} - \sqrt{R_{ro}^2 - x^2} \tag{11}$$

where R_{ro} is the outer radius of the outer ring.

Based on surface deformation of the roller and its initial geometric profile, the true geometric profile of the roller, denoted as $d_r(x)$, can be evaluated using

$$d_r(x) = R_r - \sqrt{R_r^2 - x^2} + v_r(x) \tag{12}$$

where R_r is the radius of the roller.

The simulation results obtained under a load of 230 N at various rotational speeds, including the associated hydrodynamic pressure and film fraction profiles, are shown in Figs. 2(b)–(e). Significant discrepancies exist between the equivalent and actual deformed profiles, as depicted in Figs. 2(b) and (c), which lead to notable variations in acoustic wave propagation, reflection, and transmission. Furthermore, the pressure distribution shown in Fig. 2(d) is used to calculate the oil density and sound velocity variations along the distance in the ultrasonic simulation. The film fraction, which is illustrated in Fig. 2(e) and derived from Eq. (5), indicates the presence of cavitation. The initial location of the cavitation region is used to determine the length of the outlet region in the following analysis.

2.2. Acoustic simulation of ultrasonic reflection under EHL conditions

A high-fidelity acoustic simulation model is developed to investigate the effects of EHL conditions on ultrasonic reflection, as shown in Fig. 3. The model simulates the propagation of ultrasonic waves in a rolling bearing using COMSOL Multiphysics software. Two modules are used to capture the overall reflection behavior across the contact region: A linear elastic module is used to model steel deformation, and an acoustic pressure module with a line source is used to simulate the normal incidence of ultrasonic waves. The specific steps that are conducted to establish the finite element simulation model of the acoustic field are as follows:

Step 1: geometric model;
Step 2: material parameters;
Step 3: boundary conditions;
Step 4: excitation signal;
Step 5: mesh generation;
Step 6: solving.

The geometric model, including the oil film thickness distribution and the geometric profiles of solid bodies, can be constructed from the results in Fig. 2. For simplicity, the relative motion between the roller and the ring is represented in the simulation by virtually translating the ultrasonic sensor with respect to a fixed roller. This treatment is mathematically equivalent to the actual condition in which the roller passes beneath a fixed sensor and does not affect the validity of the simulation results. The sensor movement direction and the oil film distribution are shown in Fig. 3(a). An acoustic simulation is conducted on the basis of four variables: the inlet region length, the outlet region length, the rotational speed, and the load. In addition, the pressure distribution obtained from the numerical simulation is used to determine the local sound speed and density at various positions, which are then applied as parameters for the acoustic model. A detailed explanation of Steps 2–6 is provided in Ref. [12].

For each sensor position, the time-domain echo signals are transformed into the frequency domain using fast Fourier transform (FFT), which yields the corresponding reflected frequency signals. The reflection coefficient is then calculated as the amplitude ratio between the echo signal and a reference signal that is obtained by simulating the oil film as an air medium. A controlled variable method is used to investigate the effect of each factor on the ultrasonic reflection coefficient:

(1) Effect of the outlet region length. The changes in the reflection coefficient with the sensor-to-contact distance for various oil film outlet lengths are shown in Fig. 3(b), with the inlet region length fixed at 3 mm, the rotational speed set to 400 revolutions per minute (rpm), and the load set to 230 N. When both the outlet and inlet regions are fully lubricated (i.e., equal to 3 mm), the EHL results in a characteristic "double-peak–single-valley" pattern in the reflection coefficient distribution. The two side peaks are symmetrical, and the central valley is relatively pronounced.

The peak value within the outlet region increases and then decreases as the length of the outlet region decreases, and it is consistently higher than the peak value in the inlet region. The peak value in the inlet region remains relatively unchanged as the length of the outlet region decreases, but it suddenly increases when the length of the outlet becomes comparable to the sensor width (approximately 0.3 mm). Additionally, near the contact area (approximately –0.5 to 0.5 mm), as the outlet length decreases, a slight "collapse" occurs toward the right of the central region, which causes the valley to shift toward the outlet side. When the outlet region gradually decreases to 0.13 mm, which is the initial position of cavitation determined by the EHL simulation, "collapse" occurs toward the right of the central region, which causes the valley to shift toward the outlet side. Moreover, the reflection coefficient that corresponds to the central oil film thickness increases as the length of the outlet region decreases.

(2) Effect of the inlet region length. The changes in the ultrasonic response relative to the sensor-to-contact center distance for various inlet lengths of the oil film are shown in Fig. 3(c), with the length of the outlet region set to 0.13 mm and the rotational speed set to 400 rpm. As the length of the inlet region decreases, the peak value within the inlet region gradually increases, whereas the outlet peak on the right side changes minimally. When the length of the inlet region approaches the sensor width, the peak value within the inlet region gradually decreases, and at the same time, the peak value in the outlet region on the right side begins to increase. Additionally, the variation in the length of the inlet region has a relatively minor effect on the reflection coefficient at the center of the contact area.

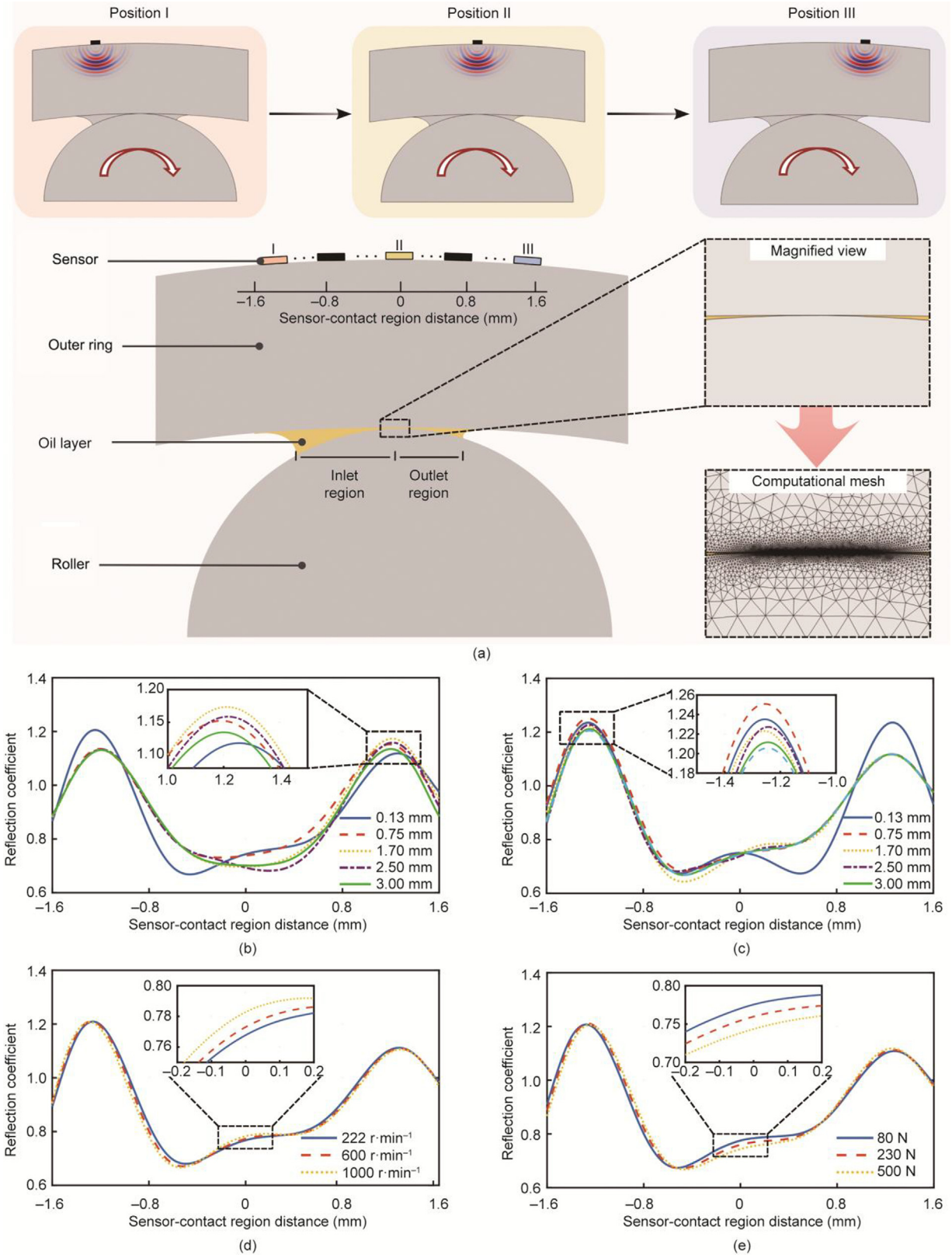

Fig. 3. Acoustic simulation of ultrasonic reflection under EHL conditions. (a) Geometric model of the roller–outer ring contact; (b) effect of the outlet region length on the reflection coefficient, with fixed values for the other parameters; (c) effect of the inlet region length on the reflection coefficient, with fixed values for the other parameters; (d) effect of the rotational speed on the reflection coefficient, with fixed values for the other parameters; (e) effect of the load on the reflection coefficient, with fixed values for the other parameters.

(3) Effect of the rotational speed. The changes in the ultrasonic response relative to the sensor-to-contact center distance under various rotational speeds are shown in Fig. 3(d), with the load set to 230 N. The reflection coefficient near the contact region

(approximately –0.5 to 0.5 mm) gradually decreases as the rotational speed increases.

(4) Effect of the load. The changes in the ultrasonic response relative to the sensor-to-contact center distance under various loads when the rotational speed is set to 400 rpm are illustrated in Fig. 3(e). The reflection coefficient near the contact region (approximately –0.5 to 0.5 mm) gradually increases as the load increases. This may be because of cavitation, which generates air–oil interfaces on the lubricant side and air–steel interfaces on the outer ring side. These additional interfaces introduce extra ultrasonic reflections, thus modifying the simple trend. Consequently, the reflection coefficient near the contact region increases overall with both increasing load and rotational speed.

The following conclusions can be drawn from the above analysis: ① In the absence of cavitation, the reflection coefficient distribution exhibits a "double-peak–single-valley" pattern that is shaped by the combined effect of the contact geometry and the EHL-induced oil film thickness distribution. The two side peaks are symmetrical, and the central valley is relatively pronounced. ② The presence of cavitation increases the reflection coefficients that correspond to the central oil film thickness. A slight "collapse" occurs toward the left of the central region, which causes the valley to shift toward the inlet side. ③ The decrease in the length of the inlet region causes the side peak in the inlet region to first increase and then decrease but has a minimal effect on R_c. ④ Under different loading and rotational speed conditions, the general trend of the reflection coefficient distribution curves remains consistent. However, owing to the presence of cavitation, R_c increases with increasing rotational speed and load.

2.3. Central oil film thickness extraction

The peak values in both the outlet and inlet regions are approximately symmetrical under varying inlet lengths, outlet lengths, loads, and rotational speeds. Therefore, the symmetric center between the two peaks is used to locate the extraction point to accurately obtain R_c. Additionally, the length of the inlet region has a minimal effect on this reflection coefficient. The deformation profile along with the initial cavitation location can be determined via EHL simulation. Increases in the applied load and rotational velocity lead to increases in the measured reflection coefficient that corresponds to the central lubricant film. Thus, the extraction method for the central film thickness can be realized via EHL and acoustic simulations. The procedure is outlined below:

Step 1: EHL simulations are performed to calculate the deformation profile, contact pressure distribution, and cavitation initiation location of the roller–outer ring contact area under various operating conditions (e.g., load and speed).

Step 2: On the basis of the results of the acoustic simulations, an acoustic model for the roller–outer ring system is established to obtain the reflection coefficient $R_{fz(center)}$ in the central region and the overall sensor reflection coefficient R_{fz} under various operating conditions.

Step 3: To define a mapping between these two reflection coefficients, a correct factor R_g is introduced:

$$R_g = \frac{R_{fz(center)}}{R_{fz}} \tag{13}$$

Step 4: A polynomial fitting method is used to establish a relationship between the adjustment factor and operating parameters. Under the assumption that the fitting model is an nth order polynomial, the relationship is expressed as follows:

$$R_g = \sum_{i=0}^{n} a_i U^i L^{n-i} \tag{14}$$

where a_i represent the fitting coefficients and i denotes the index corresponding to each polynomial term (typically ranging from 0 to n). Furthermore, U represents the rotational speed, and L represents the load. By using the least squares method or other fitting techniques, the coefficients a_i can be determined, and the most suitable polynomial order n can be selected on the basis of the fitting accuracy that is required for the actual data. This polynomial may include linear, quadratic, and interaction terms, with the degree n chosen on the basis of the data fitting accuracy.

Step 5: In actual measurements, when the reflection coefficient R_{sc} that is obtained from sensor data is known, together with the bearing dimensions, load, and speed, the corresponding correct factor R_g for the operating conditions can be determined from the polynomial fitting results. The reflection coefficient R_c in the contact area can subsequently be calculated as follows:

$$R_c = R_{sc} \cdot R_g \tag{15}$$

Step 6: Using the corrected reflection coefficient R_c, the average film thickness h_{cen} in the contact zone can be obtained using the spring model method [21,22]. The formula is as follows:

$$h_{cen} = \frac{B}{2\pi f z_1 z_3} \sqrt{\frac{R_c^2 (z_1 + z_3)^2 - (z_1 - z_3)^2}{1 - R_c^2}} \tag{16}$$

Although the raw reflection coefficient does not follow classical film thickness trends with speed and load, the proposed coupled elastohydrodynamic–acoustic framework allows precalibration and correction. EHL simulations provide the contact deformation, pressure distribution, and cavitation location, whereas acoustic simulations yield the central reflection coefficient. A correction factor (R_g) removes non-film-related contributions, so the calibrated central reflection coefficient (R_c) accurately represents the oil film, and the extracted thickness follows the expected EHL trend of increasing with speed and decreasing with the load.

3. Experiments

To validate the effects of EHL deformation, outlet region length, and inlet region length on ultrasonic reflection, an experiment was first conducted on a rolling bearing test rig using a glass–oil–steel configuration—with a glass outer ring and steel rollers. The glass outer ring enables optical observation of the oil film distribution variation via fluorescence, thus facilitating comparison with the measured reflection, although the lower acoustic impedance of glass reduces the sensitivity of the ultrasonic signal to film thickness variations. The results were compared with the trend analysis derived from the simulation to support the interpretation of the mechanism. A steel–oil–steel configuration—with both the outer ring and rollers made of steel—was subsequently used to further quantitatively validate the accuracy of the proposed central film thickness extraction method under realistic bearing conditions by comparing the measured results with those of theoretical EHL calculations.

3.1. Experiments with a glass–oil–steel configuration

The experimental setup and results for the glass–oil–steel bearing configuration used to verify ultrasonic reflection mechanisms under EHL conditions are shown in Fig. 4. The test rig used a cylindrical roller bearing, Model N208, with its outer ring replaced by a glass ring of the same size without a raceway but with a coating. The lubricant film on the inner cylindrical surface of the glass outer ring was visualized using a fluorescence-based method. In this technique, a fluorescent dye is added to the lubricant, and the film is illuminated with ultraviolet light. The emitted fluorescence intensity is directly correlated with the local film thickness,

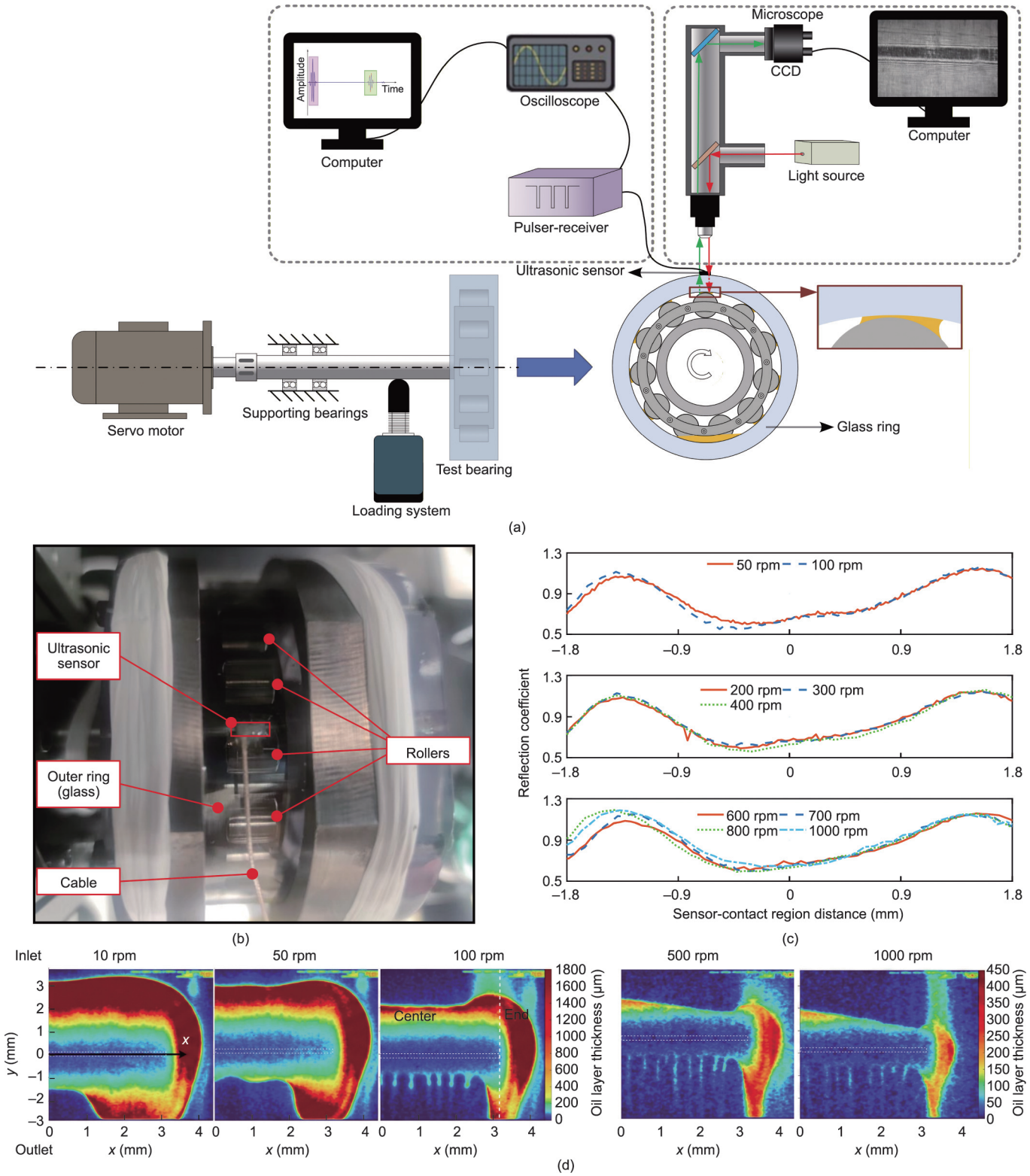

Fig. 4. Experimental setup and results for the glass–oil–steel bearing configuration used to verify ultrasonic reflection mechanisms under EHL conditions. (a) Schematic illustration of the test rig setup with ultrasonic and optical fluorescence measurements integrated; (b) installation of the ultrasonic sensor for *in situ* measurement in the glass bearing setup; (c) measured reflection coefficients under various rotational speeds using PAO4 oil; (d) optical fluorescence measurements under various rotational speeds using PAO8 oil, adapted from Ref. [4], which are used for comparison and validation of the ultrasonic reflection measurements. CCD: charge-coupled device.

thereby enabling quantitative measurement through prior calibration [4].

An image of the attachment of the ultrasonic sensor to the glass outer ring of the bearing is shown in Fig. 4(b). The ultrasonic sensor used was a rectangular piezoelectric ceramic sensor, which had been encapsulated and wired for stability. To facilitate both optical observation and the attachment of the ultrasonic piezoelectric ceramic sensor, the measurement position of the ultrasonic sensor

was located at the uppermost roller. A rectangular sensor was installed with its short edge perpendicular to the rolling direction and its long edge parallel to the line contact region, with the roller ensured to pass directly beneath the active sensing area during operation. In the experiment, the sensor remained fixed at this position, and the roller moved beneath it. Therefore, the ultrasonic signals that were recorded at different instants naturally corresponded to different relative positions between the roller and the sensor.

The specific experimental procedure was as follows: A servo driver was used to control the motor for precise speed control of the inner ring of the bearing, with the rotational speed range in the experiment being 50–1000 rpm. A loading screw was used to apply radial loads in a vertically downward direction. Since the load had a minimal effect on the lubricant film thickness, the maximum pressure at this measurement point was maintained at 0.18 GPa, the contact area width was 80 μm, and the room temperature was constant at 23 °C during the experiment. The lubricant used in the experiment was of model polyalphaolefin 4 (PAO4), with a dynamic viscosity of 0.027 Pa·s. During the experiment, a pipette was used to add a precise 1 mL of lubricant to the bottom of the inner cylindrical surface of the outer ring, with the lubricant ensured to be evenly distributed across the surfaces of the outer ring, rollers, and inner ring by driving the bearing.

The measurement results for the ultrasonic reflection coefficient during the passage when the roller moved at different speeds (50–1000 rpm) under the same load conditions (PAO4 oil) are shown in Fig. 4(c). As shown in Fig. 4(c), between −1.5 and 1.5 mm, the overall shape exhibits a "double-peak–single-valley" pattern. The left peak, which corresponds to the inlet region, occurs within −1.6 to −1.2 mm, whereas the right peak, which corresponds to the outlet region, occurs within 1.2–1.6 mm. As the rotational speed increases, the peak amplitude of the inlet region remains nearly unchanged, whereas the peak amplitude of the outlet region increases, particularly in the exit area. Additionally, the minimum point consistently appears within the inlet region length.

The oil film thickness distribution that was measured using the fluorescence method (PAO8 oil) with a glass outer ring is shown in Fig. 4(d). The glass allowed optical observation of the oil film, although its lower acoustic impedance reduced the sensitivity of ultrasonic reflection to thickness variations. As the rotational speed increased, the length of the inlet region decreased, and cavitation appeared in the outlet region, with the cavitation position changing little. The length of the inlet region was always greater than that of the outlet region.

These experimental results confirm the trend that was predicted by the simulation: A decrease in the length of the inlet region leads to an increase in the reflection coefficient of the inlet region (Fig. 4(c)). In the experiment, the increase in speed effectively decreased the inlet length, which corresponded to the observed increase in the inlet-region reflection coefficient, thus demonstrating consistency between the simulation and experiment. Although PAO4 and PAO8 have different viscosities, the qualitative trend of the inlet-region reflection coefficient with changing inlet length in the simulation corresponds to the trend that was observed experimentally with varying rotational speed, thus supporting the validity of the comparison.

3.2. Experiments with steel–oil–steel configurations

A rolling and sliding test rig was used to validate the ultrasonic measurement technique of the bearing with the steel outer ring and steel rollers (Fig. 5). The rolling and sliding test rig consisted primarily of a test bearing, loading system, servo drive system, industrial control computer, and lubrication system. The operating principle was as follows: The loading system applied a load to the outer ring of the bearing while keeping the outer ring fixed in place. The industrial control computer controlled the servo motor, which rotated the inner ring of the bearing at various speeds. Lubrication oil was sprayed by a peristaltic pump onto the rollers and outer ring, thereby ensuring lubrication of the contact area. The test bearing model was a standard bearing with a flanged outer ring, model NF211EM. In the experiments, the slip ratio was set to 0, and the rollers underwent pure rolling motion. A total of 12 operating conditions were set, where the loads on the rollers at different measurement points were 86.25, 143.75, and 230 N, respectively; and the inner ring speeds were 166.5, 222, 277.5, and 333 rpm, respectively.

A comparison between the simulated and measured reflection coefficient distributions when the load was 230 N and the speed was 333 rpm is shown in Fig. 5(b). The simulated reflection coefficient distribution matches well with the measured results at the first peak in the inlet region and the first peak within the outlet region. The discrepancies arose from multiple sources, with the primary deviation likely because of the simplified and idealized setting of cavitation in the simulation. In reality, the cavitation shape is much more complex and features not only oil–gas transition regions but also "fern cavities" or "oil strips" [23]. These irregularities in the oil distribution can significantly affect ultrasonic wave reflections and introduce errors into the results.

The central oil film thickness measurement results across various operating conditions are shown in Fig. 5(c). When the overall reflection coefficient of the sensor was directly used in the spring model formula to estimate the film thickness, the deviation relative to the EHL theoretical prediction was the greatest. In contrast, the proposed method produced oil film thickness measurements that closely aligned with EHL theoretical predictions under various operating conditions, with a maximum error of 12.7%. Therefore, the proposed method achieved higher measurement accuracy. Additionally, as shown in Fig. 5(d), the measurement results for different rollers fluctuated under identical operating conditions. This could have been because of signal interference and fluctuations in the measurement instruments, vibrations of the test rig, or inconsistencies in roller manufacturing.

4. Discussion

The proposed ultrasonic method provides a high-resolution, *in situ* approach for measuring the central oil film thickness in rolling element bearings. By combining ultrasonic measurements with EHL simulations and acoustic modeling, the relationship between the ultrasonic reflection coefficient and the film thickness can be established, and the real deformation profile, contact pressure distribution, and cavitation effects can be fully accounted for. Compared with traditional spring-model calculations, this approach provides a more accurate measurement of the central film thickness in the contact area. Despite these advantages, several limitations remain to be addressed in future work.

(1) Physical and operational limitations. This study focused on line contact bearings, specifically cylindrical roller bearings, as the rectangular sensor was designed to cover the line contact region. Although the method is generally applicable to different materials and lubricants, the sensitivity of the measurement to film thickness may vary because of differences in the acoustic impedance between the solid-bearing material and the lubricant. Extreme operating conditions, such as lubrication starvation or severe defects in the races or rolling elements, may reduce measurement accuracy because of local anomalies in the oil film and altered reflection signals. Improving measurement accuracy under such extreme conditions will be considered in future work.

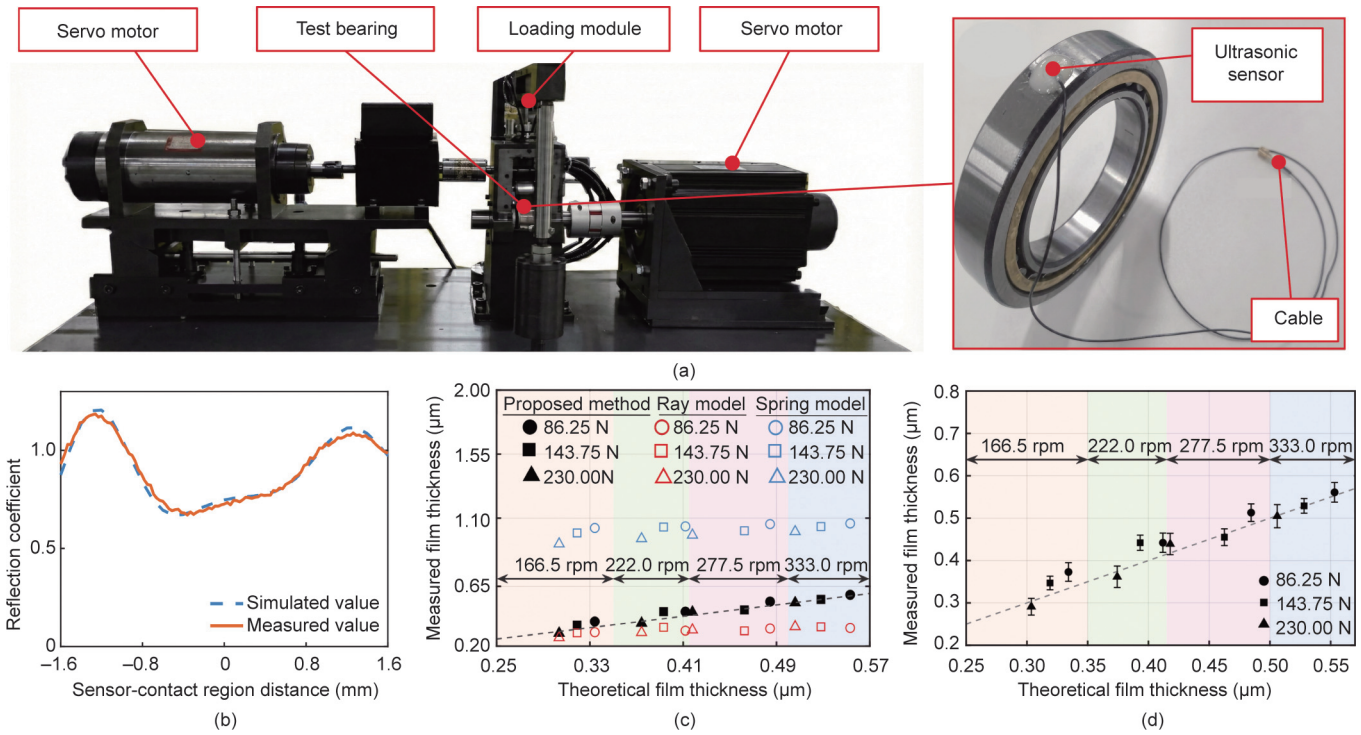

Fig. 5. Experimental validation of central film thickness extraction using a steel–oil–steel bearing configuration. (a) Photograph of the bearing test rig with a steel outer ring and steel rollers; (b) comparison between simulated and experimentally measured reflection coefficient distributions at a load of 230 N and a speed of 333 rpm; (c) comparison of central film thickness measurement results obtained by different methods; (d) central film thickness values measured using the proposed method for 10 different rollers under identical operating conditions.

(2) Applicability to other bearing platforms. The mapping relationship between the reflection coefficient and central film thickness that was obtained in this study is valid only for the specific bearing and operating conditions that were used in the experiments. To apply the method to other bearing types, new numerical simulations under the relevant operating conditions are needed. A potential solution is to express the results in a nondimensional form, such as normalized film thickness or dimensionless contact length, which will be considered in future work to generalize the method.

5. Conclusions

To obtain high-resolution oil film thickness measurements in rolling bearings, numerical elastohydrodynamic–acoustic modeling was adopted in this study to interpret reflected ultrasound data under complex EHL conditions. Key findings indicate the following: ① Without cavitation, the reflection coefficient distribution shows a typical "double-peak–single-valley" shape, with nearly symmetrical side peaks and a relatively deep central valley. ② Cavitation shifts the valley toward the inlet region side and increases R_c. From these observations, the symmetric center between the two peaks was used to determine the extraction point for R_c. A method for extracting central film thickness was established by combining EHL and acoustic simulations under different operating conditions, thereby enabling accurate extraction of the central film thickness.

Experimental validation through both glass–oil–steel and steel–oil–steel bearing setups confirmed the effectiveness of the proposed method. The results for the glass–oil–steel configuration, which were compared against fluorescence measurements, validated the simulation-based analysis of the reflection coefficient distribution. For the steel–oil–steel configuration, the effectiveness of the method was further confirmed by comparing the extracted central film thickness with theoretical EHL calculation results. Compared with the traditional approach, the proposed method significantly reduced the measurement errors, with a maximum error of 12.7%, thus demonstrating a substantial improvement in measurement accuracy.

CRediT authorship contribution statement

Pan Dou: Writing – original draft, Validation, Methodology, Investigation, Funding acquisition, Conceptualization. **Yayu Li:** Validation, Investigation, Formal analysis. **Suhaib Ardah:** Methodology, Software, Visualization. **Tonghai Wu:** Writing – review & editing, Supervision, Funding acquisition, Conceptualization. **Min Yu:** Writing – review & editing, Methodology. **Thomas Reddyhoff:** Supervision, Methodology, Investigation, Funding acquisition. **Yaguo Lei:** Funding acquisition, Conceptualization. **Daniele Dini:** Funding acquisition, Conceptualization.

Declaration of competing interest

The authors declare that they have no known competing financial interests or personal relationships that could have appeared to influence the work reported in this paper.

Acknowledgments

Pan Dou and Tonghai Wu gratefully acknowledge the financial support from the National Natural Science Foundation of China (52405597 and 52275126). Suhaib Ardah and Daniele Dini would like to acknowledge the support received from the Engineering and Physical Sciences Research Council, United Kingdom (EPSRC) via the InFUSE Prosperity Partnership (EP/V038044/1). Daniele Dini acknowledges the support of the Royal Academy of Engineering (RAEng) for the Shell/RAEng Research Chair in Complex Engineering Interfaces.

References

[1] Cheng C, Ma G, Zhang Y, Sun M, Teng F, Ding H, et al. A deep learning-based remaining useful life prediction approach for bearings. IEEE/ASME Trans Mechatron 2020;25:1243–54.
[2] Yuan Y, Ma G, Cheng C, Zhou B, Zhao H, Zhang HT, et al. A general end-to-end diagnosis framework for manufacturing systems. Natl Sci Rev 2020;7:418–29.
[3] Cao-Romero-Gallegos JA, Taghizadeh S, Aguilar-Rosas OA, Dwyer-Joyce RS, Farfan-Cabrera LI. The effect of electrical current on lubricant film thickness in boundary and mixed lubrication contacts measured with ultrasound. Friction 2024;12:1882–96.
[4] Liang H, Lu Y, Wang W, Sun Y, Zhao J, Guo Y. An experimental study on the distribution of grease in cylindrical roller bearings. Lubricants 2024;12:145.
[5] Dou P, Jia Y, Zheng P, Wu T, Yu M, Reddyhoff T, et al. Review of ultrasonic-based technology for oil film thickness measurement in lubrication. Tribol Int 2022;165:107290.
[6] Mills R, Vail JR, Dwyer-Joyce R. Ultrasound for the non-invasive measurement of internal combustion engine piston ring oil films. Proc Inst Mech Eng J 2015;229(2):207.
[7] Tacconi J, Shahpar S, King A, Olufeagba JP, Khan R, Sant I, et al. Elasto–hydrodynamic model of hybrid journal bearings for aero-engine gear fuel pump applications. J Tribol 2022;144:31604.
[8] Du F, Hong J, Xu Y. An acoustic model for stiffness measurement of tribological interface using ultrasound. Tribol Int 2014;73:70–7.
[9] Drinkwater BW, Zhang J, Kirk KJ, Elgoyhen J, Dwyer-Joyce RS. Ultrasonic measurement of rolling bearing lubrication using piezoelectric thin films. J Tribol 2009;131(1):011502.
[10] Clarke BP, Nicholas G, Hart E, Long H, Dwyer-Joyce RS. Loading on a wind turbine high-speed shaft gearbox bearing: ultrasonic field measurements and predictions from a multi-body simulation. Tribol Int 2023;181:108319.
[11] Nicholas G, Howard T, Long H, Wheals J, Dwyer-Joyce RS. Measurement of roller load, load variation, and lubrication in a wind turbine gearbox high speed shaft bearing in the field. Tribol Int 2020;148:106322.
[12] Dou P, Wu T, Luo Z, Yang P, Peng Z, Yu M, et al. A finite-element-aided ultrasonic method for measuring central oil-film thickness in a roller-raceway tribo-pair. Friction 2022;10:944–62.
[13] Yuan Y, Tang X, Zhou W, Pan W, Li X, Zhang HT, et al. Data driven discovery of cyber physical systems. Nat Commun 2019;10:4894.
[14] Kasolang S, Dwyer-Joyce RS. Observations of film thickness profile and cavitation around a journal bearing circumference. Tribol Trans 2008;51:231–45.
[15] Habchi W. Elastohydrodynamic lubrication (EHL). In: Habchi W, editor. Finite element modelling of elastohydrodynamic lubrication problems. Hoboken: John Wiley & Sons, Inc.; 2018.
[16] Elrod HG. A cavitation algorithm. J Lubr Technol 1981;103(3):350–4.
[17] Ardah S, Profito FJ, Dini D. An integrated finite volume framework for thermal elasto–hydrodynamic lubrication. Tribol Int 2023;177:107935.
[18] Ardah S, Profito FJ, Dini D. A comprehensive review and trends in lubrication modelling. Adv Colloids Interface Sci 2025;342:103492.
[19] Ardah S, Profito FJ, Reddyhoff T, Dini D. Advanced modelling of lubricated interfaces in general curvilinear grids. Tribol Int 2023;188:108727.
[20] Villamayor A, Guimarey MJG, Mariño F, Liñeira del Río JM, Urquiola F, Urchegui R, et al. High-pressure thermophysical properties of eight paraffinic, naphthenic, polyalphaolefin and ester base oils. Lubricants 2023;11(2):55.
[21] Dwyer-Joyce RS, Drinkwater BW, Donohoe CJ. The measurement of lubricant-film thickness using ultrasound. Proc R Soc 2003;2032:957.
[22] Reddyhoff T, Kasolang S, Dwyer-Joyce RS, Drinkwater BW. The phase shift of an ultrasonic pulse at an oil layer and determination of film thickness. Proc Inst Mech Eng 2005;219:387–400.
[23] Vlădescu SC, Ciniero A, Tufail K, Gangopadhyay A, Reddyhoff T. Looking into a laser textured piston ring-liner contact. Tribol Int 2017;115:140–53.